Reduction of variable-truncation artifacts from beam occlusion during in situ x-ray tomography

Paper

Borg, Leise; Jørgensen, Jakob Sauer; Frikel, Jürgen; Sporring, Jon

Published in:
Measurement Science and Technology

Link to article, DOI:
10.1088/1361-6501/aa8c27

Publication date:
2017

Document Version
Peer reviewed version

Reduction of variable-truncation artifacts from beam occlusion during in situ X-ray tomography

Leise Borg[1], Jakob S. Jørgensen[2], Jürgen Frikel[3], and Jon Sporring[1]

[1]Department of Computer Science, University of Copenhagen, Denmark
[2]Department of Applied Mathematics and Computer Science, Technical University of Denmark, Denmark
[3]Department of Computer Science and Mathematics, OTH Regensburg, Germany

E-mail: [1]lebo@di.ku.dk

May 2017

Abstract.

Many in situ X-ray tomography studies require experimental rigs which may partially occlude the beam and cause parts of the projection data to be missing. In a study of fluid flow in porous chalk using a percolation cell with four metal bars drastic streak artifacts arise in the filtered backprojection (FBP) reconstruction at certain orientations. Projections with non-trivial variable truncation caused by the metal bars are the source of these variable-truncation artifacts. To understand the artifacts a mathematical model of variable-truncation data as function of metal bar radius and distance to sample is derived and verified numerically and with experimental data. The model accurately describes the arising variable-truncation artifacts across simulated variations of the experimental setup. Three variable-truncation artifact-reduction methods are proposed, all aimed at addressing sinogram discontinuities that are shown to be the source of the streaks. The "Reduction to Limited Angle" (RLA) method simply keeps only non-truncated projections; the "Detector-Directed Smoothing" (DDS) method smooths the discontinuities while the "Reflexive Boundary Condition" (RBC) method enforces a zero derivative at the discontinuities. Experimental results using both simulated and real data show that the proposed methods effectively reduce variable-truncation artifacts. The RBC method is found to provide the best artifact reduction and preservation of image features using both visual and quantitative assessment. The analysis and artifact-reduction methods are designed in context of FBP reconstruction motivated by computational efficiency practical for large, real synchrotron data. While a specific variable-truncation case is considered, the proposed methods can be applied to general data cut-offs arising in different in situ X-ray tomography experiments.

Keywords: Computed tomography, in situ measurements, filtered backprojection, sinogram discontinuities, variable-truncation artifacts.

1. Introduction

1.1. In situ X-ray tomography

X-ray computed tomography (CT) has been an indispensable non-invasive imaging technique in medical imaging, non-destructive testing, materials science and numerous other areas for many years. Traditionally, an object has been subjected to X-ray CT to provide images of its (static) internal three-dimensional structure, or to study the effect of treatments such as heating by comparing an X-ray CT scan before and after the treatment. Since only an image of the sample after the treatment is obtained, such studies only provide an indirect window into the processes taking places during the treatment. In recent years, in situ X-ray CT has become an increasingly widespread technique to study processes as they happen within material samples subject to various environments such as high temperature, high pressure, controlled atmosphere, fluid flow, etc. Some noteworthy examples in materials science include studies of rock fractures during freeze-thaw cycles [1], deformation and liquid flow in aluminum alloys under temperature control [2], evolution of fatigue cracks in magnesium [3] and fracture evolution in cement under compression [4].

In many in situ X-ray CT experiments the imaging equipment is complemented by additional equipment, often called rigs, to control the in situ environment, such as furnaces, tension rigs, fluid flow tubes, etc. Often, this equipment can be arranged to remain outside the X-ray beam from source to detector to prevent any effect on the acquired data. However, in some cases this is not possible, and the X-ray beam will either pass through or be fully or partially occluded by the equipment at some of the projection angles. This results in parts of the tomographic data being either "polluted" by the additional attenuation through the equipment or, in the case of occlusion, completely missing. Depending on the severity of this effect, the resulting tomographic reconstruction may suffer from artifacts ranging from minor to completely destructive for the desired imaging task.

The present work is motivated by in situ X-ray CT studies of fluid flow through porous chalk. The experiment entails a percolation cell with four metal bars to sustain high temperature and pressure, as detailed in Section 2 and illustrated in Figure 2. At some projection angles the metal bars cause full or partial occlusion of the X-ray beam, which results in missing data and drastic streak artifacts in the reconstruction, see Figures 3 and 4. The goal of the present work is to understand the cause of these artifacts and determine methods to reduce them.

The most common reconstruction method in routine use at synchrotrons remains the filtered backprojection (FBP) algorithm due to its versatility, robustness, computational efficiency and well-understood behavior. In recent years a variety of, mainly iterative, reconstruction methods based on an algebraic imaging model and using statistical and a priori information have been proposed and potential improvements over FBP demonstrated, see e.g., [5, 6, 7, 8]. However, major challenges remain before these methods are suitable for larger datasets in practical synchrotron routine

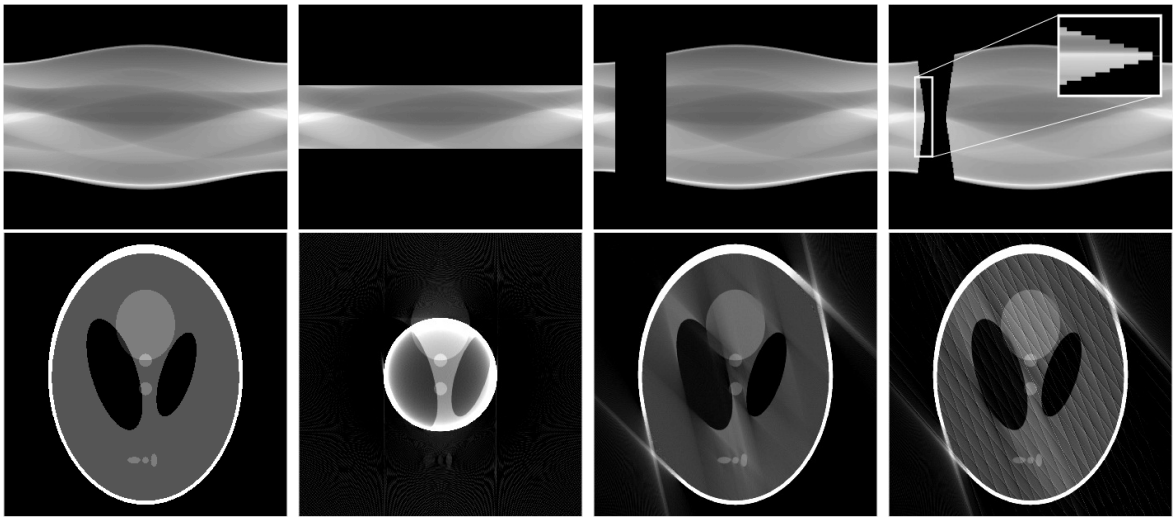

(a) Complete (b) ROI (c) LA (d) VT

Figure 1: Top row: Shepp-Logan phantom sinograms with different cut-offs. Bottom row: Corresponding reconstructions. Complete: No artifacts. ROI: Region-of-interest caused by smaller detector width than sample size. LA: Limited angle, where projections from a range of angles are missing. VT: Variable truncation, where symmetrically placed metal objects outside the sample occlude the beam causing projections with variable amount of truncation. The gray-scale window of all reconstructions is [0,0.6].

use, which often uses high resolution and thousands of projections. With these large amounts of data, the use of simple/fast algorithms is crucial. Iterative reconstrutction methods typically require computing times several orders of magnitude longer than FBP. They are more complex and typically involve tweaking of several parameters such as the number of iterations and any regularization parameters before improvements are obtained. Further, a multitude of different methods exist each with strengths and weaknesses for different types of images, making it difficult for non-specialists to choose a suitable method for a particular data set. Therefore, to be of direct relevance and easy to adopt in practice, in the present work we restrict ourselves to consider artifacts and reduction methods in conjunction with FBP reconstruction.

1.2. Typical reconstruction artifacts

A variety of reconstruction artifacts can be encountered in case of incomplete data. Figure 1 illustrates a number of typical cases with different forms of incomplete data and corresponding reconstruction artifacts. Shown first is the complete-data case without artifacts for the classical Shepp-Logan phantom. In the sinogram the columns contain projections obtained at angles from 0° to 180° in a parallel-beam configuration. Second, region-of-interest (ROI) data and artifacts arise from a smaller detector width than sample size causing projections to be truncated and detector-directed discontinuities to arise in the sinogram. The effect is a bright ring around and a pronounced cupping

artifact across the ROI. The third case is limited angle (LA) data and artifacts, where projections are missing for a range of angles, causing angular discontinuities in the sinogram and major streak artifacts emerge from edges in the reconstruction. The fourth case, which is the focus of the present work, can be seen as a combination of LA data and ROI data, in which the ROI truncation varies across projections from fully missing through partial to complete projections. In the sinogram, both angular and detector-directed discontinuities are present. The corresponding reconstruction contains LA artifacts as well as new regularly spaced streaks seemingly unrelated to image features. We refer to this case as *variable-truncation data* and *artifacts*. In this article we focus on the variable-truncation (VT) artifacts, which we will show derive from the stair-casing shape of the missing-data region in the sinogram with angular and detector-directed discontinuities, as seen in the zoom-inset in Figure 1d.

A closely related class of artifacts, mainly described in the medical imaging literature, is known as metal artifacts. Metal artifacts are often observed in medical imaging when metal is present, e.g., as implants in body parts and dental fillings. One can distinguish between two types of metal effects. First, the presence of highly-attenuating metal within tissue or bone can lead to physical effects, such as high attenuation coefficients, high noise-to-primary-signal ratio, high scatter-to-primary-signal ratio, beam hardening, and non-linear partial volume effects [9, 10]. Second, the metal edges lead to sinogram discontinuities either directly present in the raw data or user-induced, e.g., through discarding the affected data [9]. The second type of metal artifacts are very similar to the VT artifacts in that they are thin regular streaks extending tangentially from the metal edges [10, 11].

Metal-artifact reduction is often treated as missing-data problems. Typical methods are projection completion methods, which fill in missing or deteriorated data points by synthetic data [12], and algebraic reconstruction methods, which may completely omit these data points [13, 14]. Omitting single data points is not possible when using FBP, as this method needs complete projections. The methods proposed in this article provide a possibility of disregarding missing or deteriorated data in conjunction with FBP. The simplest possible idea, and the starting point for the present work, is to replace any missing data points by zero values, as illustrated in the zoom-inset of Figure 1d, simply to have complete projections without blanks in order for FBP to process the data. Doing this has two consequences:

(i) It essentially removes the first type of metal artifacts, i.e., any physical effects caused by the presence of metal which corrupts the data, as such effects primarily relate to the projection lines traversing the metal (see for instance [9] and [10] for a description of metal artifacts). This means that we do not need to account further for potential metal artifacts of this type.

(ii) It introduces discontinuities in the detector direction of the sinogram. Such discontinuities will be drastically emphasized by the filtering step of FBP to cause an artificial over- and under-shooting effect, which in turn will be back-projected

and create pronounced streak artifacts.

Many metal-artifact reduction methods are aimed at reducing these streaks by handling the discontinuities. Similarly, in the present work, we focus on addressing the discontinuities in the VT data to reduce the arising streak artifacts.

1.3. Contributions and organization of the present work

Much work has been devoted to characterize and conceive reduction methods for both LA artifacts, see, e.g., [15, 16, 17, 18, 19], and ROI artifacts [20, 21, 22, 23]. On the other hand the VT artifacts arising for the particular in situ X-ray tomography setup have to the best of our knowledge not been addressed in the literature.

To this end, the present work presents two contributions. First, after describing the experimental setup and data in Section 2, we develop in Section 3 a mathematical model of the considered setup to describe precisely how and where in the reconstruction the VT artifacts arise. The model is used to simulate VT data for variations of the experimental setup using small and large radii and distances of the metal bars, in order to describe the artifacts across a more general class of problems. We also explain that the artifacts arise from sinogram discontinuities during the filtering step of FBP.

Second, in Section 4 we propose three methods to reduce the VT artifacts – all of them simple to implement as a preprocessing step for standard FBP to allow efficient reconstruction, essential for large real synchrotron data sets. Insertion of Zeros Values (IZV) for the blank data points provides the starting point, on which we want to improve by following proposed methods:

(i) Reduction to Limited Angle (RLA), which simply discards all truncated projections to obtain an LA data set. This is a very easy way to remove the detector-directed discontinuities, but the drawback is that it discards useful data.

(ii) Detector-Directed Smoothing (DDS), which applies local smoothing to remove the detector-directed discontinuities.

(iii) Reflexive Boundary Condition (RBC), which handles the detector-directed discontinuities by imposing a reflexive boundary condition.

In Section 5 we report qualitative and quantitative results to assess the proposed methods on simulated and real VT data sets. The results show that all methods can remove the VT artifacts effectively, while DDS and especially RBC allow further reconstruction improvement by using data from the partial projections, compared to RLA, which discards this data. Finally, Section 6 discusses the methods and results in a wider context before Section 7 concludes the study.

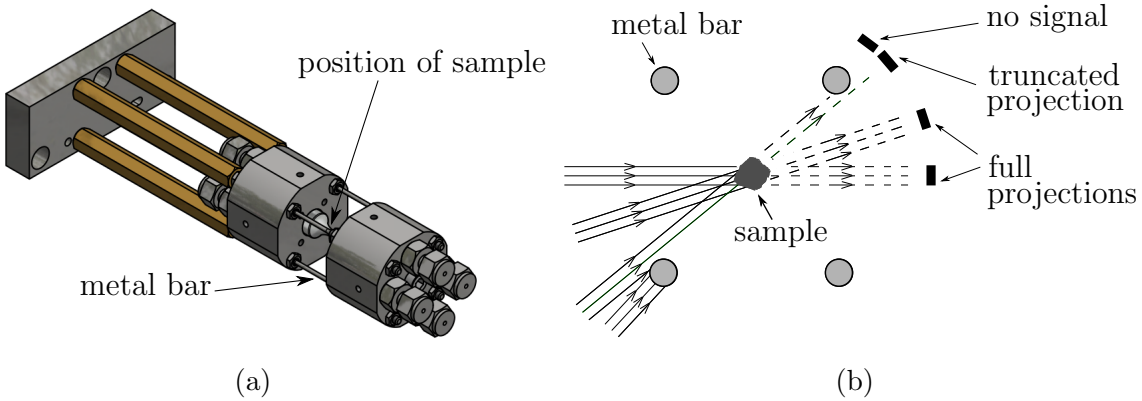

Figure 2: Left: Side-view of the percolation cell. Right: Top-view of the setup, where the specimen is placed in the center between four metal bars (not to scale). Four angular positions for the detector (the black bar) is shown: For two of them, the projections are complete. For the detector position along the SW-NE diagonal, the beam is occluded completely by the metal bars and no signal is measured at the detector. In between one position is shown at which the outermost parts of the beam are occluded by two of the metal bars, leading to a projection with truncation from both sides.

2. Data

2.1. Acquisition set-up

The motivating case for the present study is in situ X-ray micro-tomography imaging of fluid flow through porous chalk in which the goal is to recover oil from the North Sea underground. In situ X-ray tomography data was obtained for a cylindrical porous chalk sample of diameter 0.6 mm using beamline BL20XU of the SPring-8 Synchrotron Radiation Facility, Japan using a monochromatic (28 keV) parallel-beam scan configuration. Fluid is forced through the sample by a percolation cell, seen in Figure 2a, by applying a pressure of 50 bars imitating the underground conditions. The goal is to model the structural changes of the sample during the fluid flow and a series of scans are acquired continuously over the experiment. Structural changes are slow compared to the acquisition time of each complete scan and any sample deformations within each scan can be neglected. The percolation cell is equipped with four metal bars which can sustain pressures of 200 bar and temperatures of 100 °C. The metal bars have a radius of 1 mm and are positioned in a square around and at approx. distance of 15.6 mm from the sample. The number of detector pixels is 2048×2048, providing in each horizontal slice a field of view (FOV) of approx. 0.5 mm in diameter [24]. The detector is positioned outside the percolation cell and 1800 projections are collected covering 0 to 180 degrees. As seen in Figure 2b most projections are complete, some are fully occluded by the metal bars, while some projections are partially occluded. These partial projections are the focus of the present work. In addition, since the sample is larger than the FOV, all projections are slightly truncated.

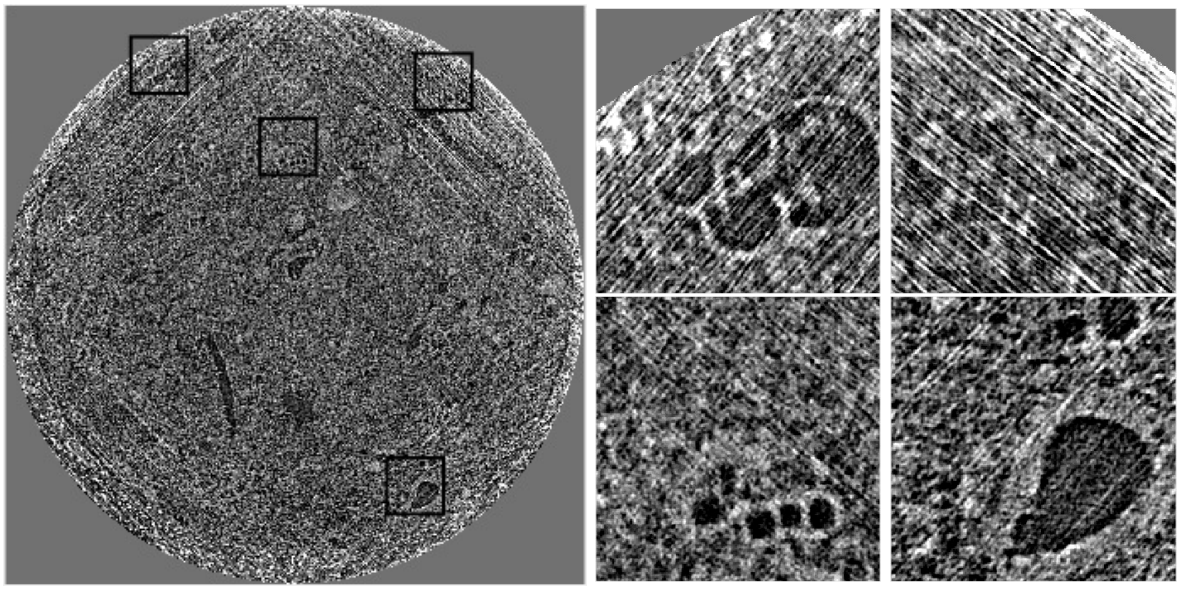

(a) (b)

Figure 3: FBP reconstruction provided by the SPring-8 synchrotron facility with zooms indicated by black squares.

2.2. Reconstruction provided by the synchrotron site

At Spring-8, FBP is used slice-by-slice to produce a 2048^3 reconstructed volume based on the acquired CT data [25]. Due to slices being independently reconstructed thanks to the parallel-beam geometry we consider without loss of generality the FBP reconstruction of a single 2048×2048-pixel slice. Artifacts are clear, especially towards the outlying region of the reconstruction, see Figure 3. They appear as streaks with angles of approx. 45 and 135 degrees measured in the counter-clockwise direction from the horizontal axis. The artifacts cause problems for subsequent analysis of the data: From the reconstruction, an automated segmentation of the chalk pores is needed as a step towards the fluid flow model. This requires a high-quality artifact-free reconstructed image. The present work is motivated by identifying the cause of the streaks and finding a way to reduce them.

2.3. Processing the raw data

From the complete raw data set the data corresponding to slice number 1000 out of 2048 is extracted and consists of 1800 projections of length 2048 pixels. These are the transmission values measured at the detector and we denote it by $I(\phi, p)$, where ϕ denotes the rotation angle and p the detector position. In addition, two flat fields $I_{0,\text{before}}$ and $I_{0,\text{after}}$ are recorded before and after $I(\phi, p)$ was recorded, i.e., with the X-ray beam on, but the sample out of the field of view, as well as a dark field I_{bg}, i.e., with the source off to account for any background radiation. Flat and dark fields are used

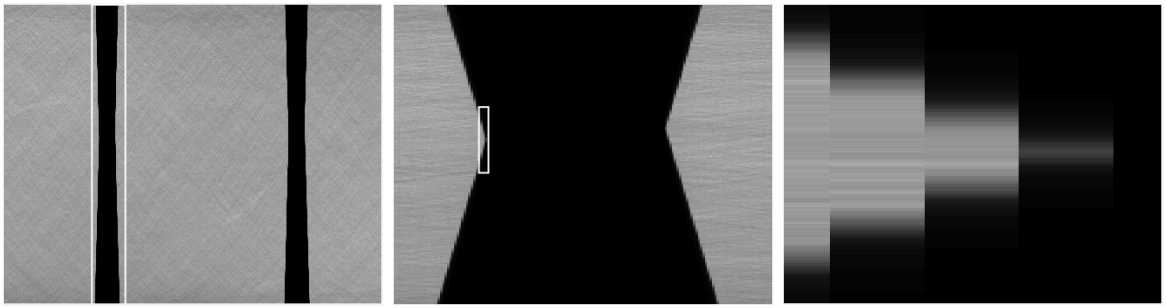

(a) Transmission sinogram. (b) Zoom 1. (c) Zoom 2.

Figure 4: Flat- and dark-field corrected sinogram $Z(\phi, p)$ and two zooms. The white rectangles in (a) and (b) denote the zoom areas in (b) and (c), respectively. Gray scale window is [0,0.53], corresponding to the fraction of photons detected.

for flat- and dark-field correction of all projections, i.e.,

$$Z(\phi, p) = \frac{I(\phi, p) - I_{\text{bg}}(\phi, p)}{I_0(\phi, p) - I_{\text{bg}}(\phi, p)}. \tag{1}$$

As the source conditions such as voltage and current may change slightly during a scan, $I_0(\phi, p)$ is an interpolated flat field calculated for each projection from the two flat fields $I_{0,\text{before}}$ and $I_{0,\text{after}}$ by weighting by projection angle:

$$I_0(\phi, p) = \left(1 - \frac{\phi}{180^\circ}\right) \cdot I_{0,\text{before}}(p) + \frac{\phi}{180^\circ} \cdot I_{0,\text{after}}(p). \tag{2}$$

Figure 4 shows the flat- and dark-field corrected sinogram $Z(\phi, p)$. It represents the number of counted photons relative to the emitted photons and is the sinogram from which the SPring-8 reconstruction in Figure 3a is calculated. The horizontal axis is projection angles, ϕ, over 0 to 180 degrees and the vertical axis is detector element position, p. Because the metal bars are positioned relatively far from the chalk sample and the detector width is small compared to the metal bar radius, the full sinogram resembles the LA sinogram in Figure 1c. However, on close inspection, as seen in the zooms of Figure 4, clear differences are apparent. Instead of the immediate transition from a full to a complete blank projection in the LA case, projections are increasingly truncated over an angular range, eventually becoming completely blank, when the beam is fully occluded, before gradually becoming decreasingly truncated again. This corresponds to the case in Figure 1d. Due to the symmetry of the metal bar positions, the patterns are symmetric around the detector center, seen in zoom 1. Taking a more narrow look at the sinogram in zoom 2, stair-casing is revealed with vertical and horizontal boundaries. In the idealized case of continuous ϕ and p, the width of the truncated projections would be decreasing or increasing continuously. Since a finite number of projections are recorded in practice, a stepwise change is observed with angular-directed discontinuities, i.e., across vertical line segments.

In the detector direction a smooth transition is seen from the full signal to zero photon counts across the detector elements in the partially occluded projections. The

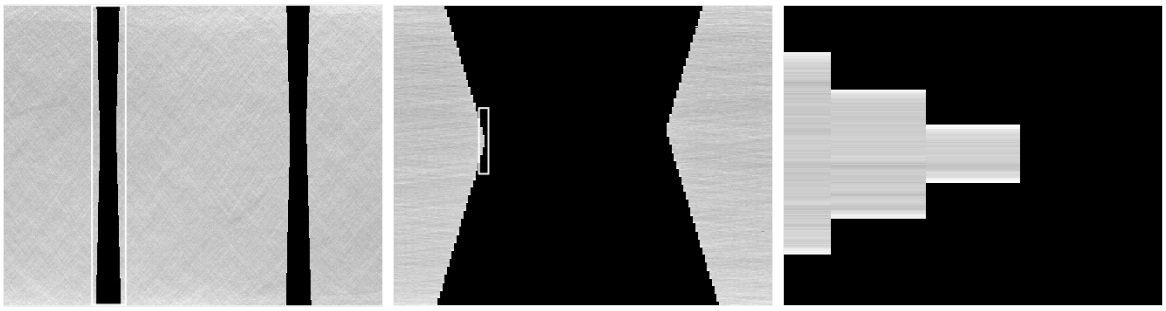

(a) Attenuation sinogram (b) Zoom 1. (c) Zoom 2.pdf

Figure 5: Sinogram $S(\phi, p)$ after negative logarithm transform and insertion of zero values in blank pixels, along with two zooms. The white rectangles in (a) and (b) denote the zoom areas in (b) and (c), respectively. Gray scale window is [0,1.43].

smooth transition indicates that the occlusion does not occur abruptly but slightly gradually over some detector pixels. The lower counts recorded in the transition region are not representative of the sample and need to be handled along with blank measurements due to beam occlusion.

2.4. Handling small or zero transmission values in FBP reconstruction

For a monochromatic X-ray beam, Lambert-Beer's law, here rewritten as

$$\int_L \mu(s)ds = -\log \frac{I}{I_0}, \tag{3}$$

where $\mu(s)$ is the linear attenuation coefficient at spatial position s to be recovered, provides a decent model of X-ray attenuation as a basis for reconstruction. Dark field and variables ϕ and p have been omitted here for simplicity. For parallel-beam data reconstruction can be done using the filtered backprojection (FBP) algorithm applied to a sinogram consisting of the right-hand side of (3) for all measured angles ϕ and detector positions p.

To arrive at such a sinogram, we need to apply the negative logarithm to $Z(\phi, p)$, and we denote the resulting sinogram as $S(\phi, p) = -\log Z(\phi, p)$. Zero- and close-to-zero values in $Z(\phi, p)$ are not handled well by this model, as they are mapped to infinity or very large values by the negative logarithm and will dominate the reconstruction [10]. Values of $Z(\phi, p) \in [0, 0.53]$ smaller than an empirically chosen threshold, 0.24, are discarded, leaving blank areas in the sinogram. FBP cannot handle pixels without an assigned value, so some values need to be assigned to complete the projections. The simplest choice, that does not make any assumptions, is to assign the value zero in the blanks of $S(\phi, p)$, resulting in the attenuation sinogram, which we still denote $S(\phi, p)$, shown in Figure 5. In practice this operation was carried out by replacing all entries of $S(\phi, p)$ for which $Z(\phi, p)$ was smaller than 0.24 by a zero. A few, less than 50, isolated pixels within the existing projections were hereby unintentionally set to zero. These pixels were assigned values by linear interpolation in the corresponding projection.

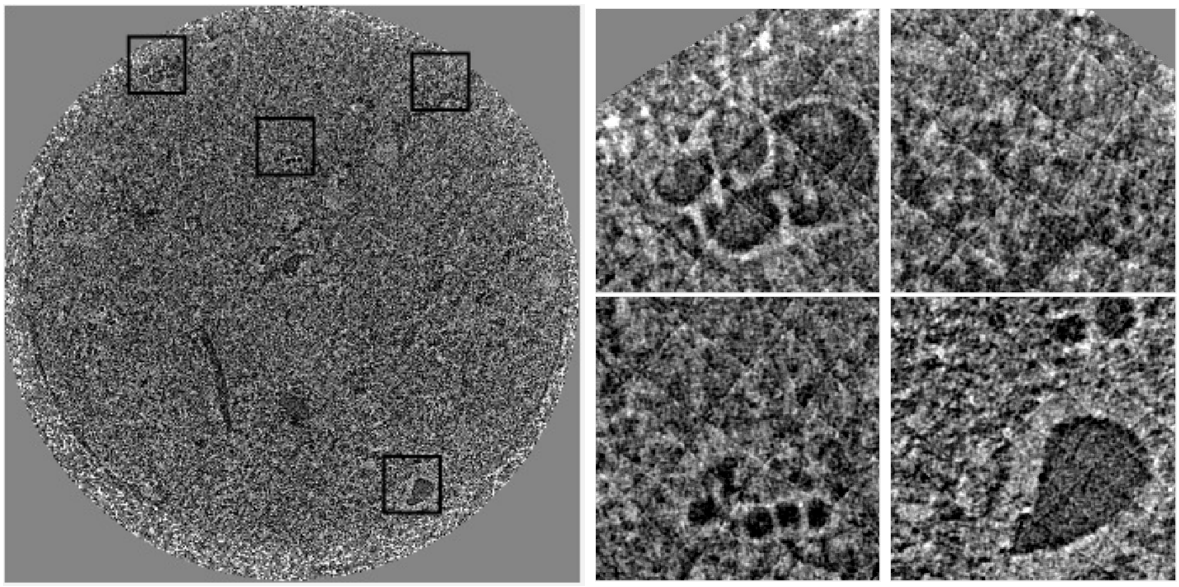

(a) (b)

Figure 6: FBP reconstruction based on the sinogram $S(\phi, p)$ with zeros inserted in blank positions, with zooms indicated by black squares.

Following this, an FBP reconstruction was computed using the `iradon` function of MATLAB R2014b employing a Hamming filter for noise reduction, see Figure 6. The FBP reconstruction is seen to contain thin streak artifacts distributed regularly over the image with angles of approx. 45 degrees and 135 degrees. As such, the streaks have some resemblance with the SPring-8 reconstruction in Figure 3, only less pronounced. As we do not have access to details of the synchrotron reconstruction method, including possible pre- and postprocessing steps, it is difficult to determine the cause of the slightly different appearance. However, since the streaks in both reconstructions occur at the same angles, we believe their origin in both cases to lie with the VT data.

As seen in Figure 5, the assignment of zero-values in $S(\phi, p)$ introduces detector-directed discontinuities in the sinogram. As we will describe further in the following section, it is these discontinuities that cause the regular streak artifacts in the FBP reconstruction.

3. Analysis

3.1. Modeling the data cut-off

In order to understand the arising VT artifacts we devise a mathematical model of the missing sinogram data caused by the metal bars. We use an indicator function $m(\phi, p)$, that we refer to as the mask, to represent whether a data point exists, $m(\phi, p) = 1$, or not, $m(\phi, p) = 0$, for $\phi \in [0°, 180°)$ and $p \in \mathbb{R}$. The case $m(\phi, p) = 0$ corresponds to those projection lines which are blocked by the metal bars. Figure 7 shows the considered

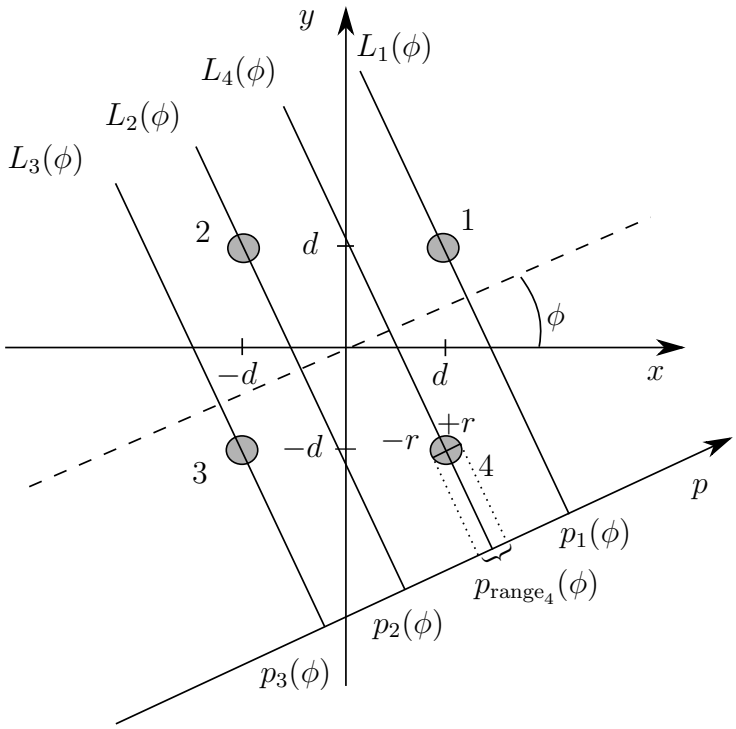

Figure 7: Metal bars 1–4 centered at (x, y)=(d, d), $(-d, d)$, $(-d, -d)$, and $(d, -d)$.

setup. Four metal bars with radius r and indexed by $i = 1, 2, 3, 4$ are positioned at $(x_1, y_1) = (d, d)$, $(x_2, y_2) = (-d, d)$, $(x_3, y_3) = (-d, -d)$ and $(x_4, y_4) = (d, -d)$, i.e., at a distance of $\sqrt{2}d$ from the origin, which is the position of the sample and assumed to be the center of rotation. The p-axis, which represents the detector, is oriented at an angle ϕ measured counterclockwise from the positive x-axis.

Each line of integration (along an X-ray) can be parametrized as a function of ϕ and p as

$$L(\phi, p) = \{(x, y) \in \mathbb{R}^2 : x \cos\phi + y \sin\phi = p\}. \tag{4}$$

The line of integration at angle ϕ which intersects the center of bar i is denoted $L_i(\phi)$. From knowledge of metal bar i's center coordinates (x_i, y_i) the corresponding p-value $p_i(\phi)$ of $L_i(\phi)$ can be found as

$$p_i(\phi) = x_i \cos\phi + y_i \sin\phi. \tag{5}$$

Using the trigonometric identity $x \cos\phi + y \cos\phi = \sqrt{x^2 + y^2} \sin(\phi + \text{atan2}(y, x))$ the expression for $p_i(\phi)$ can be simplified to a single sine function,

$$p_i(\phi) = \sqrt{2}d \sin(\phi + \phi_i), \tag{6}$$

where $\phi_i = \text{atan2}(y_i, x_i) = 45°, 135°, -135°, -45°$ for $i = 1, 2, 3, 4$.

Since the metal bar radius is r, all parallel rays within a distance of r from $L_i(\phi)$ will be blocked by metal bar i, in other words, for all p in the range

$$p_{\text{range}_i}(\phi) = \,]\, p_i(\phi) - r, p_i(\phi) + r \,[\quad \text{for} \quad i = 1, 2, 3, 4, \tag{7}$$

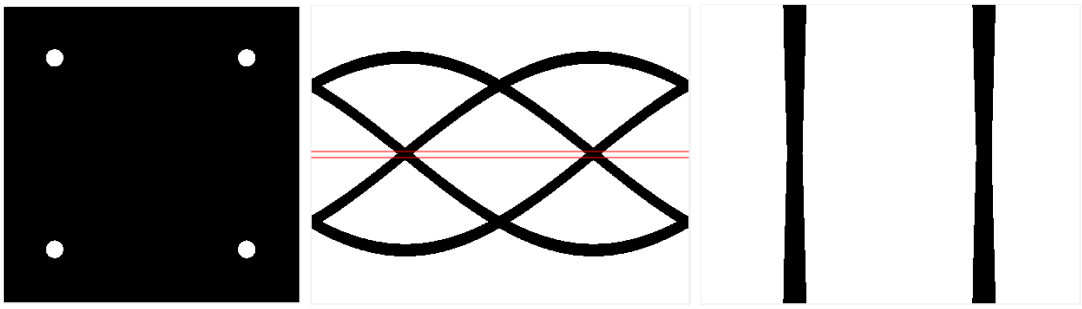

(a) (b) (c)

Figure 8: (a): Top-view of four metal bars with radius 1 mm. (b): The corresponding sinogram mask (white is 1, black is 0). The horizontal axis is projection angles, ϕ, over 0 to 180 degrees and the vertical axis is detector element position, p. The two horizontal lines denote the zoom of the sinogram to the right, imitating a detector width of 0.5 mm. (c): A zoom of the mask, which reproduces the variable truncation of projections in the real data in Figure 4.

no signal will be measured. As an example, the range $p_{\text{range}_4}(\phi)$ is sketched in Figure 7. At a fixed angle ϕ a ray will be blocked if its p-value is in (at least) one of these ranges, or equivalently, in the union of the ranges. Hence we can write the mask combining all four metal bar ranges explicitly as

$$m(\phi, p) = \begin{cases} 0 & \text{when } \; p \in \bigcup_{i=1}^{4} p_{\text{range}_i}(\phi), \\ 1 & \text{otherwise.} \end{cases} \tag{8}$$

Figure 8 shows a synthesized image consisting of four metal bars seen from above, the corresponding sinogram mask extending to fully including the metal bars, and a zoom of the mask corresponding to the actual detector width. The metal bar radius is 1 mm and the distance to the rotation center is $\sqrt{2} \cdot 11$ mm $= 15.6$ mm to closely approximate the actual experimental set-up. The full mask contains four bands of missing data, one for each metal bar. Each band has a distinct sinusoidal appearance, which is in agreement with (8), which prescribes four superpositioned sinusoidal bands of vertical thickness $2r$. Due to the symmetry of our setup, the two sets of opposite metal bars result in two pairwise crossings of the bands over the 180° range.

When the detector only covers 0.5 mm instead of the entire image, this is equal to zooming in on the sinogram, seen in Figure 8c. The zoom is indicated by the centered rectangle in Figure 8b. The missing-data region in the sinogram zoom closely resembles the motivating real-data case in Figure 4 and can be used to simulate missing data from a complete sinogram.

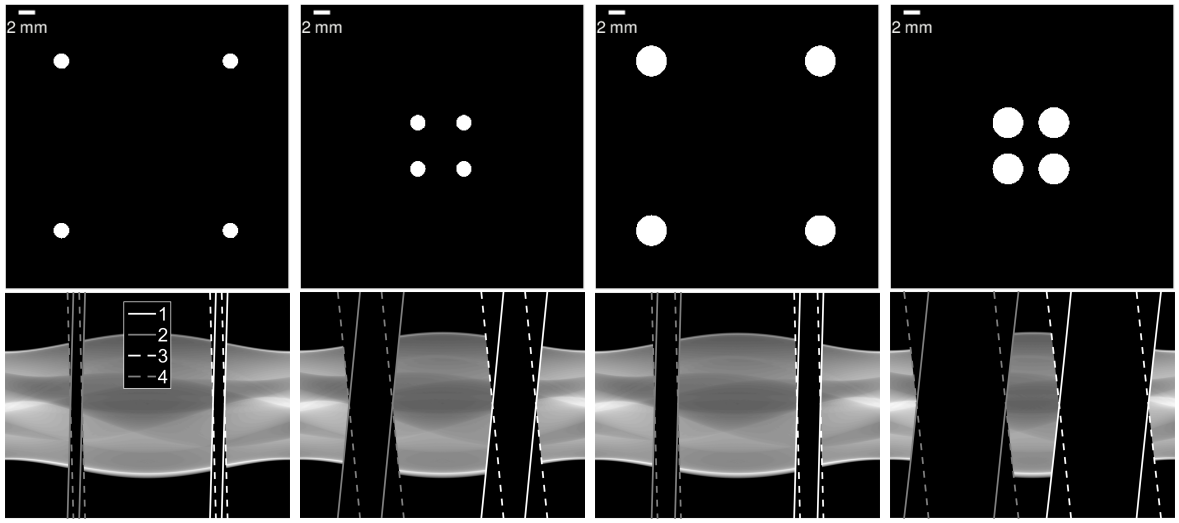

(a) Mask 1 (b) Mask 2 (c) Mask 3 (d) Mask 4

Figure 9: The top row shows images of four metal bars seen from above. Metal bar radii r and distances d are $(r, d) = (1, 11),\ (1, 3),\ (2, 11),\ (2, 3)$, respectively. This gives rise to four sinogram masks (similar to the mask shown to the right in Figure 8): Mask 1, 2, 3, and 4, which are applied to the sinogram of the Shepp-Logan phantom, shown in the bottom row. The detector width is 0.5 mm.

3.2. Varying metal bar radius and distance to object

Using the derived mathematical model we can simulate the effect of variations of the experimental setup (metal bar radius and distance) on the arising data truncation. We do this to show how the derived mathematical model describes a larger class of potentially interesting imaging scenarios with variable beam occlusion. By considering this extended set of test problems we hope to illustrate that our proposed VT artifact reduction methods can enable useful reconstructions under more challenging data truncation than that of the originally motivating case of Figure 3.

Figure 9 shows four cases of possible acquisition set-ups (combinations of radius 1 mm and 2 mm, and distance 3 mm and 11 mm) with images and corresponding masks applied to the sinogram of the Shepp-Logan phantom. To verify that the analytically computed mask expression (8) is correct, the boundary curves of the intervals in (7) as function of ϕ for all bars are plotted on top of sinogram masks simulated numerically by applying MATLAB's `radon` function to the images in the top row in Figure 9. The boundary curves follow the numerical mask boundaries exactly, and further illustrate the contribution of each of the four metal bar shadows in the sinogram.

The original case corresponds to Mask 1 and is seen to entail the smallest amount of missing data. Increasing radius at fixed distance is seen to produce a wider band of missing data, while the cut-off slope appears to be unchanged. This is in agreement with behavior predicted by (7) that the $p_i(\phi)$ follows a sine curve independent of r, while the vertical band thickness grows linearly with r, which causes a wider horizontal gap

of missing data. Increasing distance at fixed radius is seen to reduce the missing data gap width and increase cut-off steepness. This can also be understood from (7), since the sinusoidal amplitude grows linearly with d causing the derivative at the crossings to be of larger magnitude, which is equivalent to a steeper cut-off and a narrower missing data gap.

3.3. How variable-truncation artifacts arise in filtered backprojection

To understand how streaks arise, we first briefly remind the reader that reconstruction by FBP consists of two steps: Filtering and backprojection. The filtered sinogram will be referred to as $H(\phi, p)$.

Any introductory textbook on the mathematics of CT, such as [10], explains that the filtering step of FBP emphasizes discontinuities to yield very large values with opposite signs on each side of the discontinuity in the filtered projection. This is illustrated in Figure 11. Backprojecting such a filtered projection produces a pair of a dark and bright streak along $L(\phi, p)$.

A truncated projection viewed over the full projection's domain contains a discontinuity at the truncation point. If the truncation is constant over all projections, as is the case with ROI data as shown in Figure 1b, these streaks still "line up" and cancel each other out (in the continuous or highly sampled case) yielding no streak artifacts but only a circle of discontinuities at the ROI border and a cupping artifact as seen in Figure 1b. However, if truncation is not constant over all projections, as in the case in Figure 1d, the resulting streaks will no longer line up and cancel each other out. In particular, in case of a finite number of projections, the angular increment is finite and hence even a gradual truncation width change in the continuous domain is approximated by steps in the discrete practical case. This means that adjacent truncated projections have different width, which results in streaks occurring at different p-positions, preventing them from canceling with each other. The result, as shown in the following subsection, is regular streaks at certain angles across the entire reconstruction.

3.4. Streak artifacts caused by data with variable truncation

Figure 10 shows the reconstructions when applying mask 1–4 to the sinogram of the Shepp-Logan phantom. In the top row, the full reconstructions are seen, and in the bottom row, the zooms specified by the white rectangles in the top row are seen. To emphasize VT artifacts the zooms are shown in narrower gray-scale window, as specified in the figure caption. The full reconstruction images mainly show LA artifacts, i.e., few large streaks emerging from edges in the image, especially from the skull. The zooms additionally show regularly spaced VT artifacts. In the reconstructions in Figure 10, there is exactly one streak for each detector-directed discontinuity in the sinograms in Figure 9, and its angle and position depends on the position of the detector-directed discontinuity. For further discussions and illustrations of this, see [26].

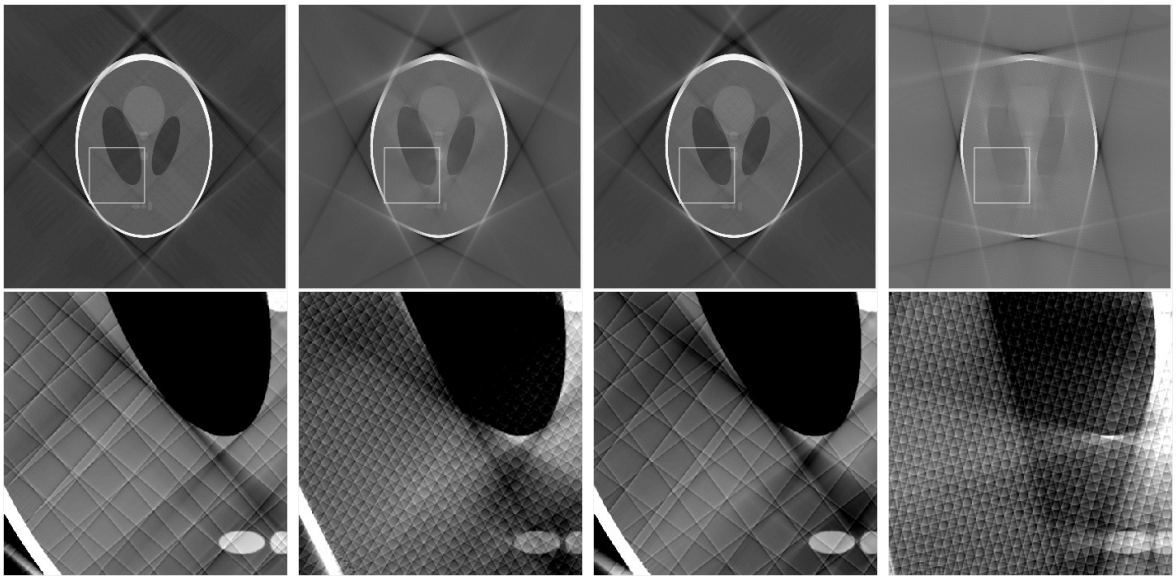

(a) Reconstruction 1 (b) Reconstruction 2 (c) Reconstruction 3 (d) Reconstruction 4

Figure 10: Reconstructions based on sinograms in Figure 9 with Mask 1, 2, 3, and 4 from left to right, respectively. The white squares indicate the positions of the zooms in the bottom row. The gray-scale windows are for the full images [-0.23,1.03], [-0.49,1.03], [-0.37,1.02], [-0.76,0.98] and the zooms [0.10,0.30], [0.05,0.30], [-0.01,0.20], [0.10,0.30], respectively. Different windows are used, since different amounts of missing data cause different reconstruction intensities.

Four different angles of streaks are seen in Reconstruction 1: either just under or just over 45 degrees or just under or just over 135 degrees. The reason of this is found in the corresponding sinogram in Figure 9 where the detector-directed discontinuities are seen to occur exactly around these angles. Because the sinogram discontinuities occur with approximately regular spacing in the p-direction, the streaks also appear regularly spaced and with angles corresponding to the angles of the truncated projections.

The streaks in case 3 have the same spacing as in case 1, because the cut-off slope is the same. However, since the detector-directed discontinuities occur farther from 45° and 135° the two sets of VT artifacts are further from being pairwise parallel.

For mask 2 and 4 the metal bars are much closer to the rotation center than for mask 1 and 3. This leads to a less steep cut-off of the data, and more plentiful detector-directed discontinuities, which again means that more densely spaced streaks are present in the reconstructions, as observed in second and fourth columns of Figure 10. As before, the streaks in case 2 and 4 occur with the same spacing but at different angles, since the detector-directed discontinuities occur at different angles.

As a final remark, we note that in each case four seemingly parallel sets of streaks can be observed, however since the detector-directed discontinuities occur over an angular range, only the streaks coming from the same projection are in fact perfectly parallel.

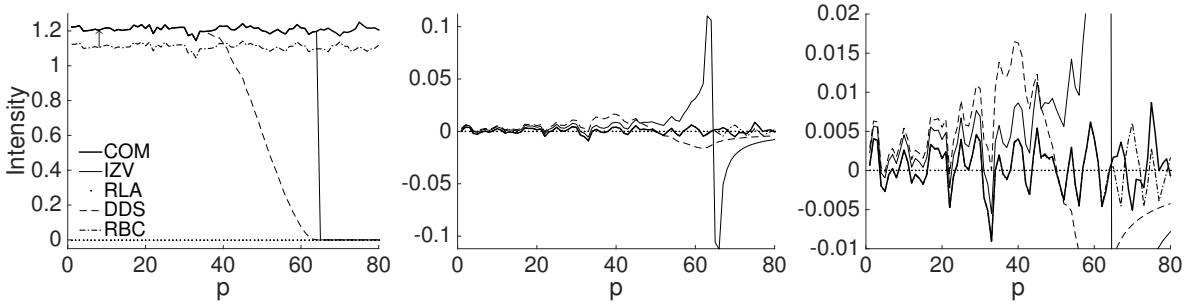

(a) (b) (c)

Figure 11: The proposed methods illustrated on a 1D truncated projection before and after filtering. Left: Projections before filtering, $S(\phi, p)$. Note, that RBC is shifted downwards for illustration purposes as indicated by the arrow and coincides with COM left of the discontinuity. Middle: Projections after filtering, $H(\phi, p)$. Right: Zoom of projections are filtering. Note that in RBC the padded values will be set to zero before backprojection, see Figure 13 for an illustration on the original data.

4. Methods

4.1. Overview of proposed methods

Having completed our analysis and description of the VT artifacts caused by detector-directed discontinuities we now proceed to propose three methods to reduce them. The proposed methods are motivated by being straightforward to implement in conjunction with FBP to allow fast reconstruction using a well-understood algorithm already in routine use at synchrotron beamlines. In the following subsections we describe each of the proposed methods but we first give a brief overview of the methods considered:

- Complete dataset (COM): In case of simulated data use the complete sinogram as "ground truth" without applying any missing-data mask.
- Insertion of Zero Values (IZV): Fill all missing data points by zeros.
- Reduction to Limited Angle (RLA): Set all truncated projections to zero, thus reduce to limited-angle problem.
- Detector-Directed Smoothing (DDS): Multiply all truncated projections with a function for local smoothing of detector-directed discontinuities.
- Reflexive Boundary Condition (RBC): Introduce a reflexive boundary condition at the detector-directed discontinuities.

Figure 11 illustrates the methods on a 1D truncated projection before (left) and after (middle and right) the filtering step of FBP. The methods RLA, DDS and RBC are motivated by handling the detector-directed discontinuities in order to reduce VT artifacts that arise when simply filling missing values by zeros in the IZV method.

4.2. IZV: Insertion of Zero Values

The simplest choice that does not make any assumptions is to assign zero values in the log-transformed sinogram domain. However, this introduces discontinuities in the truncated projection causing oscillations after filtering, as illustrated in Figure 11. Figure 11b illustrates the extreme overshoot followed by an undershoot near the discontinuity, resulting in pairs of dark and bright streaks across the reconstructed image. The overshoot even offsets long before the discontinuity, as seen in Figure 11c. Typical ROI-artifacts appear as a bright ring in the outskirts of the reconstruction (where the truncation discontinuities are), which is also explained by this effect. IZV is the starting point that we want to improve on by the following methods.

4.3. RLA: Reduction to Limited Angle

Replacing all truncated projections completely by zero values eliminates sinogram staircasing, thereby removing the detector-directed discontinuities and therefore also the VT artifacts. Setting truncated projections to zero reduces the problem to a pure LA problem, which as seen in Figure 1c and Figure 1d effectively removes streaks. In Figure 11, this method is seen as the graph which is zero for all p-values. It is the impression of the authors that RLA is in practical use among X-ray CT experimentalists as a simple method to avoid the streak artifacts caused by variable data truncation. While simple and effective, this method completely discards the potentially usable data in the truncated projections, for an example of this, see [26, Figure 19].

4.4. DDS: Detector-Directed Smoothing

This method multiplies each of the truncated projections with a function, which dampens intensity values near the detector-directed discontinuities, thereby obtaining smooth transitions, as seen in Figure 11. This method is motivated by [15, 27], where smoothing is applied in the angular direction to reduce LA artifacts. In our case we do not apply angular smoothing, but smoothing in the detector direction. At angle ϕ_0 we have a projection truncated at $p = a_0$ and $p = b_0$ in $S(\phi_0, p)$. We modify the smoothing function used in [27] for detector-directed smoothing by defining

$$g_\epsilon(p) = \left(\frac{1}{\epsilon^2} p(2\epsilon - p)\right)^2, \tag{9}$$

where ϵ specifies the width of the smoothing region, i.e., the number of pixels over which projection values will be smoothed to decay to zero, and

$$\kappa_\epsilon^{a,b}(p) = \begin{cases} g_\epsilon(p-a) & \text{if} \quad p \in [a, a+\epsilon], \\ 1 & \text{if} \quad p \in \,]a+\epsilon, b-\epsilon[, \\ g_\epsilon(p-(b-2\epsilon)) & \text{if} \quad p \in [b-\epsilon, b], \\ 0 & \text{else.} \end{cases} \tag{10}$$

Then the smoothed projection is obtained as

$$Q(\phi_0, p) = \kappa_\epsilon^{a,b}(p) S(\phi_0, p). \tag{11}$$

The function $g_\epsilon(p)$ is two times differentiable and the artifacts are two orders smoother after applying the smoothing, meaning that they are not completely smoothed, so they are mathematically still present [28]. This is in line with what we observe: After filtering of the DDS-projection, there still remain some oscillations, however substantially dampened compared to the IZV-projection, as seen in Figure 11c. We have empirically found a smoothing region of $\epsilon = 30$ pixels to provide a suitable level of smoothing and use this value throughout the presented results.

4.5. RBC: Reflexive Boundary Condition

This method introduces a reflexive boundary condition at the detector-directed discontinuities. The high-pass ramp filter in FBP emphasizes discontinuities, and the low-pass filter, e.g., a Hamming filter, often used together with the ramp filter may not dampen the oscillations sufficiently to avoid streaks. To counteract this, a reflexive boundary condition [29] is imposed to the truncated projections by padding by existing data values reflected in the discontinuity point. This induces a Neumann boundary condition with zero slope at the boundary. This method is similar to typical handling of ROI-problems where the outermost detector element values are used as padding values. After filtering of the projections, the padding is set to zero again before backprojecting, because we want to avoid introducing any artificially created data. This method works on the discontinuity itself and does not alter any existing pixel values explicitly as the RLA method and DDS methods do. As observed in Figure 11c, this is the only method that continues to coincide with the COM signal to the left of the cut-off after filtering, except for very few pixels $\simeq 4$ just before the cut-off. The discrepancy at these last few pixels is caused by the filter width in FBP: At and near the discontinuity, the filter uses pixel values from the right side of the discontinuity to calculate values to the left of the discontinuity. When reflected pixel values are used instead of pixel values from COM, this alters the pixel values left of the discontinuity.

5. Results

5.1. Overview and purpose of experiments

The proposed artifact reduction methods are assessed in the following three studies:

(i) In the original dataset in Figure 3 we want to reduce the VT artifacts to enable subsequent segmentation as part of an automated data processing pipeline designed for improving analysis of fluid flow through the pores of the chalk. The first study shows how the proposed methods perform on the original data set. Since a ground truth is not available for quantitative comparisons, we evaluate the methods qualitatively, i.e., using visual inspection.

(ii) Second, we compare the methods on the well-known Shepp-Logan phantom with simulated missing data in order to evaluate the methods in a controlled noise-free setting sufficiently simple that the effect of the different methods can be clearly seen. The four masks from Figure 9 are applied to a complete sinogram to assess the proposed methods across a range of possible experimental setups. The full-angle reconstruction will be used as the reference when assessing the methods quantitatively.

(iii) Finally, an equivalent real-data study is carried out using a separate chalk data set with a complete set of non-truncated projections acquired under comparable imaging conditions as the original truncated chalk data set. This study is included to evaluate the methods on a real, noisy, high-complexity problem, comparable to the original dataset, but with the advantage that a full-angle reconstruction can be determined and used as reference image for quantitative assessment.

5.2. Quantitative image quality assessment

The following image quality measures are chosen to evaluate the methods quantitatively:

(i) The root-mean-square error (RMSE):

$$\mathrm{RMSE} = \left(\frac{1}{NM} \sum_{i=1}^{M} \sum_{j=1}^{N} |R(i,j) - R_0(i,j)|^2 \right)^{\frac{1}{2}}, \tag{12}$$

where N and M are number of rows and columns in the images R and R_0, representing the reconstruction and the reference image, respectively. This measure is a standard measure, used for pixel-wise comparison in images.

(ii) Spectral Magnitude Distortion (SMD) [30]:

$$\mathrm{SMD} = \frac{1}{MN} \sum_{i=1}^{M} \sum_{j=1}^{N} |P_R(i,j) - P_{R_0}(i,j)|^2, \tag{13}$$

where P_R and P_{R_0} are the power spectra of the reconstruction and reference image, respectively. Since VT streaks occur with regular spacing, the power spectrum of a reconstruction with such artifacts will contain distinct pronounced peaks at particular frequencies. In addition, the streaks are discontinuous features relative to the underlying image and as such show up in the power spectrum as high-frequency components. In contrast, the power spectrum of the reference image contains only the frequencies of the underlying image, and the SMD precisely captures these differences. This measure, which is not as commonly used as the RMSE in the tomographic imaging literature, is chosen because it is particularly suited to detect changes in regular streak artifacts and hence well aligned with the purpose of the paper.

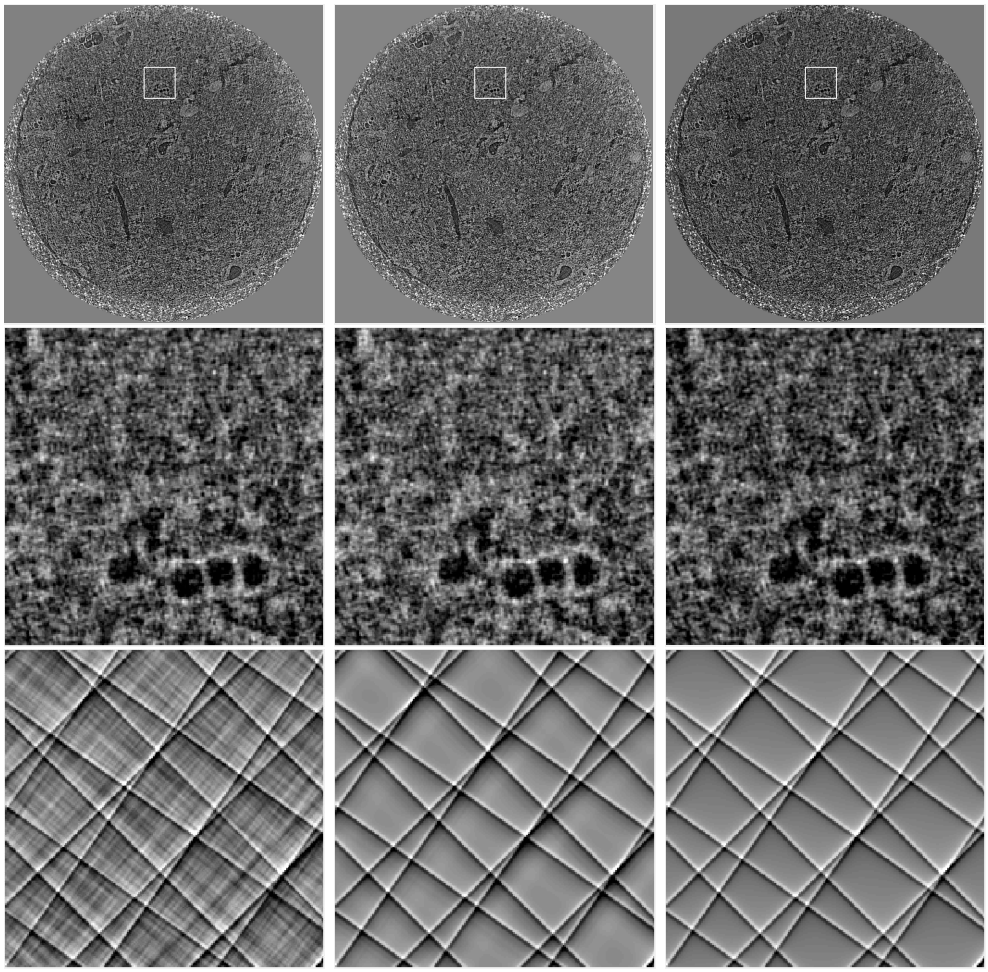

(a) RLA (b) DDS (c) RBC

Figure 12: Top row: Full reconstructed images by RLA, DDS and RBC with white squares indicating region of interest. Middle row: Zoom to region of interest. Size of region of interest is 200 by 200 pixels. Bottom row: Difference images (zoom) between the RLA, DDS, and RBC reconstructions and IZV reconstruction. Gray-scale windows are: Full reconstructions and zooms: $[-1 \cdot 10^{-4}, 10 \cdot 10^{-4}]$, difference images: $[-2 \cdot 10^{-4}, 2 \cdot 10^{-4}]$.

5.3. Original chalk dataset with variable-truncation data

Figure 12 shows the results of applying RLA, DDS and RBC to the original chalk data set with variable data truncation. The top row shows the full reconstructions for RLA, DDS, and RBC from left to right. The white squares indicate the position of a zoom to a region of interest shown in the middle row. The bottom row shows difference images between RLA, DDS and RBC and the IZV reconstruction in Figure 6b to emphasize improvements.

The top and middle rows of Figure 12 illustrate that the VT streaks are reduced to such an extent that they are no longer visible to the naked eye. Streaks, consisting

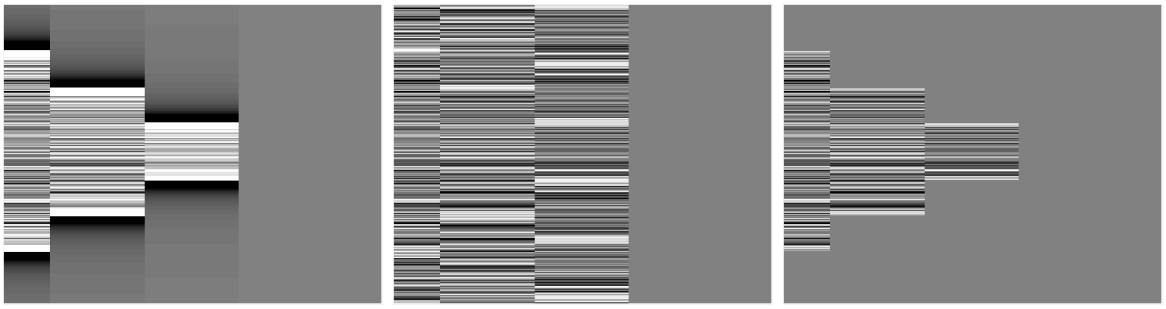

(a) IZV after filtering. (b) RBC after padding and filtering. (c) RBC after padding, filtering, and reinsertion of zeros.

Figure 13: Illustration of application of IZV (left) and RBC (center and right) on a zoom of the sinogram in the H-domain (after filtering). The left and right sinograms are the ones used when backprojecting.

of a dark and a bright line side by side, are present in all three difference images in the bottom row of Figure 12, corresponding to only being present in the IZV reconstruction. This means that they have effectively been removed by RLA, DDS and RBC. The RLA difference image has additional vague underlying streak structures with same directions of the streaks. Since these are only present here, they must correspond to the data lost when the truncated projections are set to zero. The discarded projections all correspond to angles near 45° and 135°, explaining the angles of the underlying structures. The background of the RBC difference image appears constant, whereas smooth variations appear in the gray squares for DDS. We can explain this, since RBC works only on the discontinuity itself and does not damp or enhance the projection values near the discontinuities as DDS does. In conclusion, all methods remove streaks satisfactorily, while we consider RBC to be superior to DDS, which is in turn superior to RLA, in terms of not modifying reconstruction background structure.

Given that some projections are completely missing, especially so for RLA, one could have expected LA artifacts similar to the ones in Figure 10 but none are seen. The intensity of LA streak artifacts scale with the contrast between the features from which they emerge [28]. Unlike the Shepp-Logan phantom, which contains large contrasts and thus clear LA artifacts, the chalk-data contrast is relatively low, which we believe can explain the absence of pronounced LA streak artifacts.

Figure 13 shows zooms of the $H(\phi, p)$ sinogram, i.e., after filtering, for IZV and RBC applied to the original dataset. Figure 13a illustrates the projections of IZV after filtering, just before backprojection. The extreme overshoot/undershoot shown in Figure 11 is also seen in this image. In the missing-data region next to the discontinuities of the truncated projections, the pixels are very dark (undershoot), while just within the existing-data region the pixels are very bright (overshoot). Figure 13b shows the same part of the sinogram for RBC with reflexive padding and after filtering, while Figure 13c further shows when zeros have been reinserted in place of the padding prior

to backprojection. We note that detector-directed discontinuities remain in the RBC sinogram and will thus be backprojected. However, they do not generate VT artifacts in the RBC reconstruction in Figure 12. This emphasizes that it is the filtering step of FBP that leads to streaks from detector-directed discontinuities, whereas the backprojection step does not.

5.4. Simulated variable-truncation data using the Shepp-Logan phantom

The four different masks are applied to the Shepp-Logan sinogram. As was seen in Figure 10, the IZV reconstructions suffer from both LA and VT artifacts. RLA, DDS and RBC are applied to the four cases and zooms of reconstructed images are shown in Figure 14 along with the same zoom for IZV repeated for ease of comparison.

RLA, DDS and RBC reconstructions all show substantial reductions of VT artifacts. Because of the phantom simplicity, the noise-free simulation study and the use of a narrow gray-scale window, differences between the methods are highlighted, and the LA artifacts stand out clearly.

The DDS method does not remove the streaks as successfully as the other methods do, which is most clear when comparing the reconstructions in the first and third columns. Figure 11c shows that the DDS signal still has an overshoot followed by and undershoot near the discontinuity. In other words, DDS smooths the discontinuities meaning that it also smoothies the streaks and dampens their effect, but does not remove them completely. There is a trade-off such that if ϵ is too small, streaks are not sufficiently reduced, and if too large, streaks are reduced but too much of the actual image is lost as well.

Comparison of the reconstructions in the fourth column illustrates that DDS and RBC have fewer LA artifacts than RLA has: The black blob in the reconstructions would have been an ellipse if data were not missing; the blob in the RLA reconstruction is larger, less closed and more smeared than for DDS and RBC, because more data has been erased in the RLA method. Similarly, the small bright ellipse in the bottom-right corner is more well-defined for DDS and RBC than for RLA. Comparable observations can be made for the three other cases but to a lesser extent since data truncation is most severe in the fourth case.

RLA removes all detector-directed discontinuities completely, meaning that VT artifacts are not present in RLA reconstructions. The RBC reconstructions are similar to the RLA reconstructions in that no streaks are visible, indicating that RBC removes – or at least substantially reduces – the VT artifacts. RBC thus has fewer LA artifacts than RLA and better streak reduction than DDS and from a qualitative perspective the results render it the superior method of the three.

For quantitative assessment, Table 1 reports RMSE and SMD values for IZV, RLA, DDS and RBC applied to the four cases. The computed values are global, i.e., computed over the full reconstruction images using the full-angle COM reconstruction as reference. In all cases, the global RMSE values are very similar for all methods and hence do not

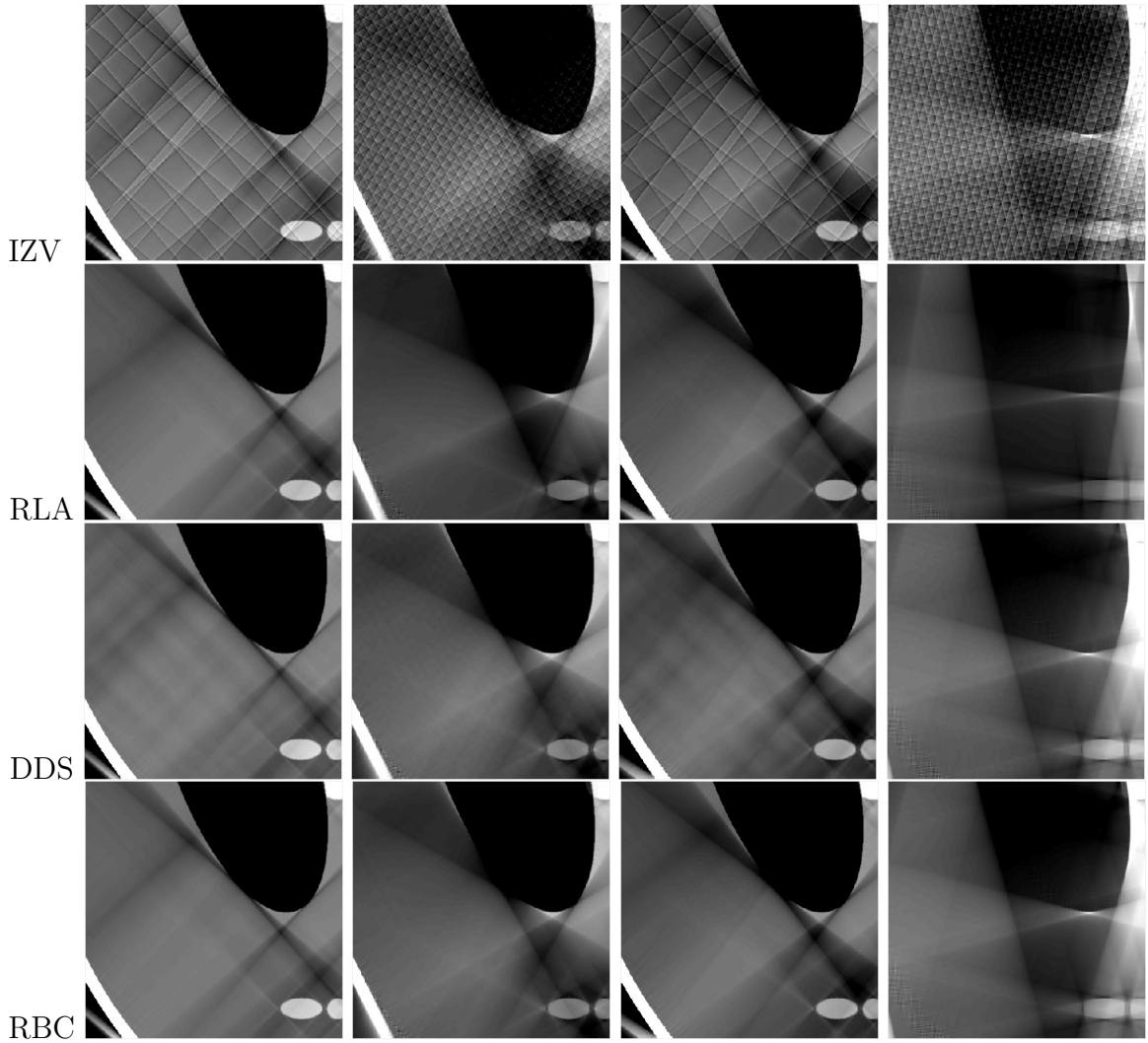

Figure 14: Shepp-Logan reconstruction zooms based on methods (vertical) and different masks imposed on the sinogram (horizontal). The position of the zooms are shown in Figure 10. Gray-scale windows are [0.10,0.30], [0.05,0.30], [-0.01,0.20], and [0.10,0.30] for the reconstructions in columns 1 to 4, respectively.

reflect the visual assessment that all methods improve over the IZV method: In terms of global RMSE, RLA appears to worsen the reconstruction, while DDS and RBC only offer marginal gains. The global SMD measures, on the other hand, are in better alignment with the visual assessment, confirming RBC as the best performing method. We believe the discrepancy for RMSE is due to quite large differences between the full-angle reconstruction and any of the other reconstructions caused by the missing data and LA artifacts. The improvements that RLA, DDS, and RBC offer in terms of RMSE are so small compared to the global quality drop from the full reconstruction to either of the missing-data reconstructions, that they may be completely dominated by other artifacts. Measuring the RMSE only over a smaller region, where LA artifacts are not

	RMSE				SMD			
	Mask 1	**Mask 2**	**Mask 3**	**Mask 4**	**Mask 1**	**Mask 2**	**Mask 3**	**Mask 4**
IZV	0.0422	0.0930	0.0634	0.1361	5.3092	17.0283	8.5020	27.3855
RLA	0.0461	0.1043	0.0669	0.1478	4.3620	15.1321	7.5844	26.0166
DDS	0.0416	0.0922	0.0631	0.1356	3.7973	12.8935	6.9873	23.4302
RBC	0.0414	0.0925	0.0630	0.1364	3.7827	12.8449	6.9641	23.3903

Table 1: Quantitative image quality results for IZV, RLA, DDS and RBC reconstruction from simulated variable-truncation data of the Shepp-Logan phantom. RMSE and SMD values are computed over the entire reconstructed image using the full-angle COM reconstruction as reference image.

	RMSE				SMD			
	Mask 1	**Mask 2**	**Mask 3**	**Mask 4**	**Mask 1**	**Mask 2**	**Mask 3**	**Mask 4**
IZV	0.0385	0.1038	0.0567	0.1607	0.0955	0.2381	0.1319	0.2905
RLA	0.0132	0.0374	0.0132	0.0368	0.0450	0.1059	0.0439	0.0947
DDS	0.0101	0.0174	0.0102	0.0185	0.0355	0.0666	0.0348	0.0696
RBC	0.0098	0.0195	0.0099	0.0211	0.0345	0.0679	0.0346	0.0719

Table 2: Same as Table 1 but RMSE and SMD values are computed locally over only the region of interest shown in the zooms in Figure 14.

dominating, may better capture the reduction of VT streaks.

We therefore replace the global measures by computing RMSE and SMD locally over the zooms in Figure 14 and report values in Table 2. These local RMSE results are in all cases much better aligned with the visual assessment, indicating an improvement by RLA over IZV, and further improvements by DDS and RBC. Similar conclusions are obtained for local SMD. In general, the measures do not indicate a noteworthy difference between DDS and RBC. However, as a consistent trend, RBC performs marginally better when Mask 1 and 3 are applied, whereas DDS performs a little better when Mask 2 and 4 are applied. The reconstructed images indicate that RBC is superior to DDS for Mask 1 and 3, while DDS and RBC reconstructions with Mask 2 and 4 appear of comparable quality. Overall, the quantitative results support the previous conclusion that RBC is the best performing method.

5.5. Simulated variable-truncation data using complete chalk data set

In addition to the original chalk data set with VT data we have access to a comparable but complete chalk data set without data truncation. We can use this data set to simulate data truncation as we did for the synthetic Shepp-Logan phantom in order to assess the proposed methods on a real data set with the same complexity as the original truncated chalk data. Crucially, by using the complete chalk data, we can determine a

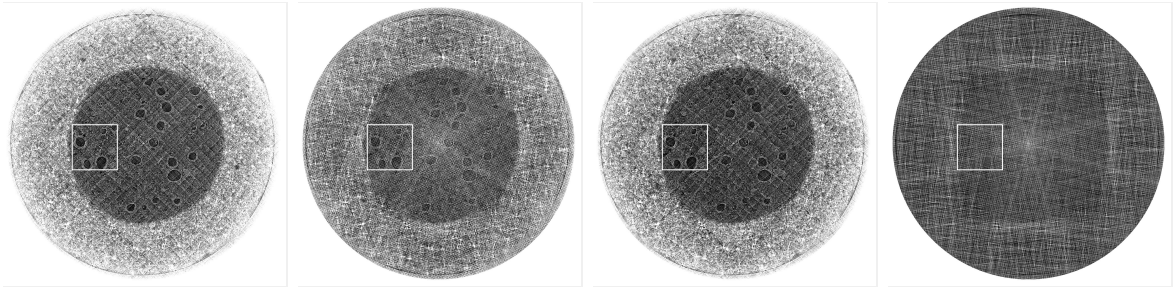

(a) Mask 1 (b) Mask 2 (c) Mask 3 (d) Mask 4

Figure 15: Reconstructions from sinograms in Figure 9, with varying radii and distances. The white squares indicate the zooms in Figure 16. Gray-scale windows are [$1.0{\cdot}10^{-4}$, $6.0{\cdot}10^{-4}$], [0, $6.0{\cdot}10^{-4}$], [$-1.0{\cdot}10^{-4}$, $6.0{\cdot}10^{-4}$], and [$1.0{\cdot}10^{-4}$, $6.0{\cdot}10^{-4}$] for each of the columns 1 to 4, respectively – the same as in the zooms of Figure 16.

full-angle FBP reconstruction for use as reference image in quantitative assessment.

Applying the four different sinogram masks, e.g., applying IZV to the complete sinogram and reconstructing from this, gives images with VT artifacts, seen in Figure 15 and zoom-ins to a region of interest in the top row of Figure 16. In particular, we note the similarity of the streaks occurring for mask 1 to the ones in the original truncated data set seen in Figure 6, for which the experimental setup (metal bar radius and distance to sample) are comparable.

After applying methods RLA, DDS, and RBC, the streaks are reduced as seen in Figure 16. Visually, all three methods improve on the IZV method. Due to noise it is difficult to see differences in the performance of the methods. However, for the second and especially the fourth column, DDS and RBC reproduce the dark round objects substantially better than RLA, for which objects are distinctively more square-like. The data cut-off in case 2 and 4 is flatter, meaning that more projections are truncated and thus discarded by RLA. It therefore makes sense that the largest advantage of DDS and RBC over RLA is seen in these cases.

Quantitative results in the form of local RMSE and SMD values are reported in Table 3 calculated only over the zooms shown in Figure 16 using the full-angle chalk reconstruction as reference. Both RMSE and SMD values are in alignment with the Shepp-Logan study in that RLA improves compared to IZV, while DDS and RBC provide further (and comparable) improvements.

We emphasize that the fourth case was deliberately chosen to be very challenging, which is reflected in the severe LA artifacts. Nevertheless, DDS and RBC manage to remove the VT artifacts and preserve the main features. Hence, DDS and RBC may in specific cases, where a coarse reconstruction is sufficient for the relevant imaging task, enable a successful imaging experiment in the face of severe beam occlusion.

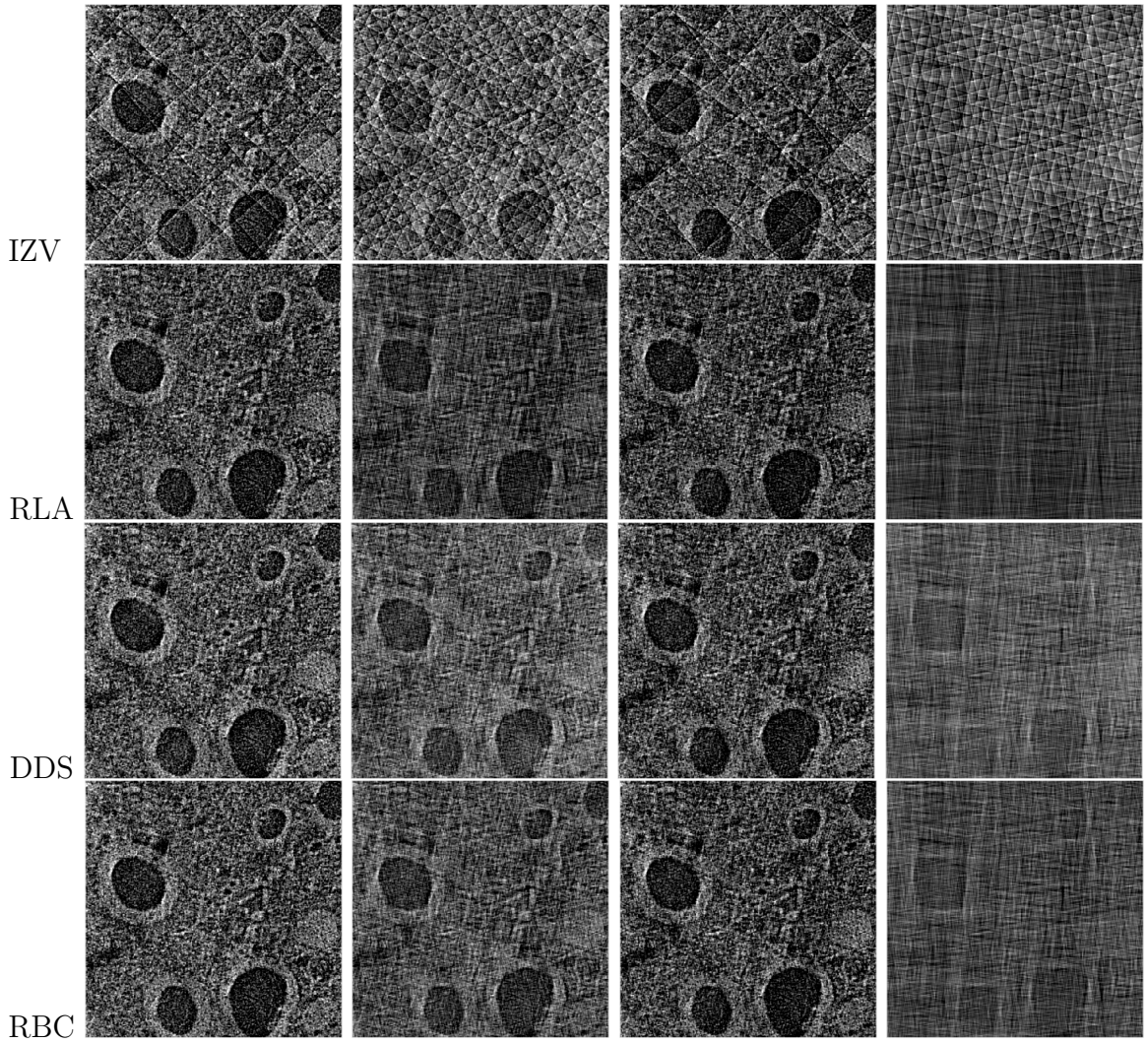

Figure 16: Mask 1, 2, 3, and 4 imposed to full dataset of chalk, reconstructed by use of methods IZV, RLA, DDS, and RBC. Zoom to region of interest of size 409 x 409 pixels. The gray-scale windows are the same as those for the full reconstruction in Figure 15.

	RMSE				**SMD**			
	Mask 1	**Mask 2**	**Mask 3**	**Mask 4**	**Mask 1**	**Mask 2**	**Mask 3**	**Mask 4**
IZV	0.0628	0.1274	0.0789	$0.1845 \cdot 10^{-3}$	0.2790	0.7042	0.3798	$1.0406 \cdot 10^{-3}$
RLA	0.0550	0.1188	0.0557	$0.1357 \cdot 10^{-3}$	0.2215	0.4917	0.2241	$0.5190 \cdot 10^{-3}$
DDS	0.0514	0.0932	0.0518	$0.0977 \cdot 10^{-3}$	0.1956	0.3899	0.1994	$0.4009 \cdot 10^{-3}$
RBC	0.0489	0.0966	0.0492	$0.1069 \cdot 10^{-3}$	0.1901	0.3869	0.1929	$0.3982 \cdot 10^{-3}$

Table 3: Quantitative image quality results for IZV, RLA, DDS and RBC reconstruction from simulated variable-truncation data using the complete chalk data set. RMSE and SMD values are computed locally over only the region of interest shown in the zooms in Figure 16 using the full-angle COM reconstruction as reference image.

6. Discussion

The results show that in all considered cases DDS and RBC outperform RLA. As the VT data cut-off becomes increasingly steep, i.e., for metal bars being further away from the sample, the number of VT artifacts is reduced as the data approaches the LA case without data truncation. In these cases, RLA discards only a small amount of data and the relative advantage of DDS and RBC over RLA diminishes, and at a certain point one may obtain equally good results by RLA.

In the other extreme, as the distance of the metal bars to the sample is decreased, the data cut-off becomes less steep and many, possibly all, projections will suffer from variable truncation. In this case RLA will have few, or even no, projections available, and therefore only allow a very poor reconstruction, if one at all. DDS and RBC, on the other hand, will be able to use the truncated projections and continue to produce a reconstruction. An indicative example of this was seen using Mask 4 in Figure 14d and Figure 15d, but for thinner metal bars closer to the sample, the cut-off will be even flatter and result in a larger advantage of DDS and RBC over RLA.

A typical answer to streaks in CT reconstructions is to increase the number of angular steps [10]. To illustrate the effect hereof on VT artifacts, we used 2, 4, 8, 16, and 32 times the number of projections originally used, namely 1800, and reconstructed from the Shepp-Logan sinogram with simulated VT by Mask 1 from Figure 9a. The top row in Figure 17 shows zooms of sinograms with different numbers of projections. The bottom row shows zooms of the corresponding reconstructions, to be compared with Figure 10a. The number of streaks doubles, when the number of projection doubles, however with weakened strength for each projection number increase. Approximately 16 times more projections are needed to smooth out the VT artifacts. The streaks may eventually cancel, but even with 32 times more projections ($32 \cdot 1800 = 57{,}600$ projections) at the considered resolution of 2048, vague shadows from the VT artifacts are still present as seen in the zoom inset of Figure 17e. In practice, one cannot always increase the number of projections due to experimental constraints, e.g., one may wish to keep acquisition time down to enable doing more scans within an allocated beam time. For a fixed acquisition time, one could increase the number of projections while reducing exposure time of each projection accordingly. However, this would reduce the signal to noise ratio in each projection and thus reduce reconstruction quality. In practice a trade-off is chosen when setting up the scan (which was out of our control) and any VT artifacts have to be dealt with subsequently.

In the present work we deliberately restricted our focus to reconstruction using the FBP algorithm to avoid increasing reconstruction time and complexity. It is quite likely that algebraic or regularization-based reconstruction methods can be developed to achieve further improvements. However, this may entail longer development time, more difficult integration in beamline reconstruction software, as well as longer computing time. We leave this for future investigations.

We also did not investigate sinogram inpainting methods, but focused on enabling

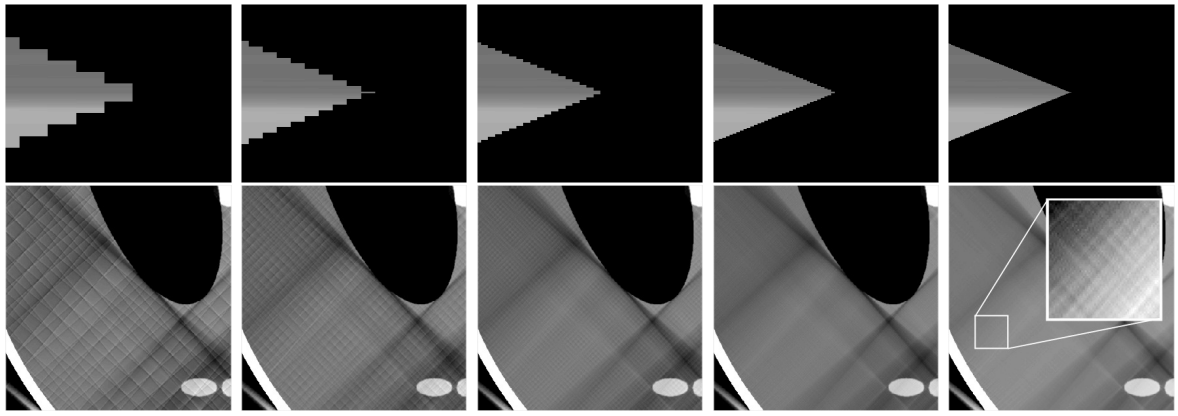

(a) $2 \cdot 1800$ (b) $4 \cdot 1800$ (c) $8 \cdot 1800$ (d) $16 \cdot 1800$ (e) $32 \cdot 1800$

Figure 17: Top row: Zooms of Shepp-Logan phantom sinograms with varied number of angular measurements as indicated below each experiment. The zooms are as in Figure 4c, all in the angular range of 41.1 to 41.5 degrees. The number of projections varies in each sinogram in that each step corresponds to one projection. Bottom row: Zooms of corresponding reconstructions. The zooms are as in Figure 10. Gray-scale window of the reconstructions is [0.4,0.12]. A zoom inset in the figure (e) is seen with increased constrast (gray-scale window is here [0.71,0.8].), indicating that vague shadows of the VT artifacts are still present.

use of all the existing data through handling of the sinogram discontinuities, without introducing artificial data which might produce new and more subtle artifacts. Nevertheless, a comparison of the methods proposed here with sinogram inpainting methods is an interesting future direction.

The proposed methods are completely automatic requiring no user input, with the sole exception of setting the threshold value below which to discard data values. This value is highly dependent on the data set and should be chosen to preserve as much of the data as possible, while discarding unreliable data. Through analysis of a histogram of the sinogram values it should be possible to determine a suitable threshold automatically, but developing a robust method for this was beyond the scope of the present work.

In the present work we focused on the detector-directed discontinuities to reduce VT artifacts, while leaving LA artifacts unreduced. We believe a straightforward extension would be to combine the methods proposed here with LA reduction techniques such as the angular smoothing proposed in [15] to achieve simultaneous LA and VT artifact reduction.

While the analysis and mathematical model for VT data developed are specific for a parallel-beam configuration, the same principles can be used to model other cases such as a cone-beam geometry which will also experience streaks from VT data. The proposed artifact reduction methods are not tied to the parallel-beam geometry and can be directly applied to other configurations. The methods are also not specific to

the particular data cut-off but applicable to general data cut-offs, including asymmetric truncation, internal gaps and combinations hereof. As such, the methods may be capable of reducing VT artifacts across a range of in situ X-ray tomography setups.

7. Conclusion

In an in situ X-ray tomography experiment of fluid flow in porous chalk the reconstructed cross sections were found to suffer from drastic streak artifacts with certain preferred directions. The streaks were found to arise from detector-directed discontinuities in the sinogram introduced by variable truncation of projections caused by partial occlusion of the X-ray beam by four metal bars of the percolation cell used in the experiment. A mathematical model describing variable truncation as function of metal bar radius and distance to sample was derived and verified numerically and in comparison with the experimental data. Using the mathematical model, the origin and location of variable-truncation artifacts were established.

Three methods for variable-truncation artifact reduction were proposed addressing in different ways the detector-directed discontinuities; by discarding all truncated projections (Reduction to Limited Angle), by smoothing the discontinuities (Detector-Directed Smoothing) and by enforcing a zero derivative at the discontinuities (Reflexive Boundary Condition).

All methods successfully reduced the streak artifacts in the original variable-truncation chalk data set. In more extensive tests across a range of simulated variable-truncation data cases using both synthetic and real data, the Reflexive Boundary Condition method was found to outperform the other methods in terms of both qualitative and quantitative assessment of reconstruction image quality. The advantage of this method and the Detector-Directed Smoothing method was found to be larger in more challenging cases involving larger proportion of truncated projections.

The proposed artifact-reduction methods are conceptually simple, computationally efficient and intended to be easy to incorporate with existing FBP implementations and apply to large real synchrotron data sets. The methods can handle quite general data cut-offs and may enable successful reconstruction across a variety of conceivable in situ X-ray tomography experiments with partial beam occlusion leading to variable-truncation data.

8. Acknowledgements

JSJ was supported by the project “High-Definition Tomography” funded by Advanced Grant No. 291405 from the European Research Council. We thank the Japan Synchrotron Radiation Research Institute for the allotment of beam time on beamline BL20XU of SPring-8 (Proposal 2015A1147). Valuable and constructive discussions with Robinson professor Eric Todd Quinto has been a great help in the development of this research work. Also, we would like to thank the P-cubed and CINEMA projects for

providing data and the very vaulable help provided by associate professor Henning Osholm Sørensen.

References

[1] T. De Kock, M. A. Boone, T. De Schryver, J. Van Stappen, H. Derluyn, B. Masschaele, G. De Schutter, and V. Cnudde. A pore-scale study of fracture dynamics in rock using x-ray micro-CT under ambient freeze–thaw cycling. *Environmental Science & Technology*, 49(5):2867–2874, 2015.

[2] B. Cai, P. D. Lee, S. Karagadde, T. J. Marrow, and T. Connolley. Time-resolved synchrotron tomographic quantification of deformation during indentation of an equiaxed semi-solid granular alloy. *Acta Materialia*, 105:338–346, 2016.

[3] A. King, W. Ludwig, M. Herbig, J.-Y. Buffière, A. A. Khan, N. Stevens, and T. J. Marrow. Three-dimensional in situ observations of short fatigue crack growth in magnesium. *Acta Materialia*, 59(17):6761–6771, 2011.

[4] Z. Yang, W. Ren, R. Sharma, S. McDonald, M. Mostafavi, Y. Vertyagina, and T. J. Marrow. In-situ x-ray computed tomography characterisation of 3d fracture evolution and image-based numerical homogenisation of concrete. *Cement and Concrete Composites*, 75:74–83, 2017.

[5] E. Y. Sidky and X. Pan. Image reconstruction in circular cone-beam computed tomography by constrained, total-variation minimization. *Physics in Medicine and Biology*, 53(17):4777–4807, sep 2008.

[6] K. J. Batenburg and J. Sijbers. DART: A practical reconstruction algorithm for discrete tomography. *IEEE Transactions on Image Processing*, 20(9):2542–2553, 2011.

[7] H. Gao, H. Yu, S. Osher, and G. Wang. Multi-energy CT based on a prior rank, intensity and sparsity model (PRISM). *Inverse Problems*, 27(11):115012, 2011.

[8] A. H. Andersen and A. C. Kak. Simultaneous algebraic reconstruction technique (SART): A superior implementation of the ART algorithm. *Ultrasonic Imaging*, 6(1):81–94, 1984.

[9] F. E. Boas and D. Fleischmann. CT artifacts: Causes and reduction techniques. *Imaging Med.*, 4(2):229–240, 2012.

[10] T. H. Buzug. *Computed Tomography: From Photon Statistics to Modern Cone-Beam CT*. Springer, Berlin, Germany, 2008.

[11] B. De Man, J. Nuyts, P. Dupont, G. Marchand, and P. Suetensl. Metal streak artifacts in x-ray computed tomography: Simulation study. *IEEE Transactions on Nuclear Science*, 46(3):691–696, 1999.

[12] W. J. H. Veldkamp, R. M. S. Joemai, A. J. van der Molen, and J. Geleijns. Development and validation of segmentation and interpolation techniques in sinograms for metal artifact suppression in ct. *Medical Physics*, 37(2):620–628, 2010.

[13] F. E. Boas and D. Fleischmann. Evaluation of two iterative techniques for reducing metal artifacts in computed tomography. *Radiology*, 259(3):894–902, 2011.

[14] L. Gjesteby, B. De Man, Y. Jin, H. Paganetti, J. Verburg, D. Giantsoudi, and G. Wang. Metal artifact reduction in CT: Where are we after four decades? *IEEE Access*, 4:5826–5849, 2016.

[15] J. Frikel and E. T. Quinto. Characterization and reduction of artifacts in limited angle tomography. *Inverse Problems*, 29(12):125007, 2013.

[16] J. Frikel. Sparse regularization in limited angle tomography. *Applied and Computational Harmonic Analysis*, 34(1):117–141, 2013.

[17] A. H. Delaney and Y. Bresler. Globally convergent edge-preserving regularized reconstruction: an application to limited-angle tomography. *IEEE Transactions on Image Processing*, 7(2):204–221, 1998.

[18] M. Persson, D. Bone, and H. Elmqvist. Total variation norm for three-dimensional iterative reconstruction in limited view angle tomography. *Physics in Medicine and Biology*, 46(3):853, 2001.

[19] M. Rantala, S. Vanska, S. Jarvenpaa, M. Kalke, M. Lassas, J. Moberg, and S. Siltanen. Wavelet-based reconstruction for limited-angle x-ray tomography. *IEEE Transactions on Medical Imaging*, 25(2):210–217, 2006.

[20] F. Noo, R. Clackdoyle, and J. D. Pack. A two-step Hilbert transform method for 2d image reconstruction. *Physics in Medicine and Biology*, 49(17):3903–3923, 2004.

[21] Y. Zou, X. Pan, and E. Y. Sidky. Image reconstruction in regions-of-interest from truncated projections in a reduced fan-beam scan. *Physics in Medicine and Biology*, 50(1):13–27, 2005.

[22] M. Müller and G. R. Arce. Truncation artifacts in tomographic reconstructions from projections. *Applied Optics*, 35(20):3902–3914, 1996.

[23] G. Van Gompel. *Towards Accurate Image Reconstruction from Truncated X-Ray CT Projections*. PhD thesis, University of Antwerp, Antwerp, The Netherlands, 2009.

[24] Y. Yang, S. S. Hakim, S. Bruns, K. N. Dalby, K. Uesugi, S. L. S. Stipp, and H. O. Sørensen. Wormholes grow along paths with minimal cumulative surface. *In preparation*, 2016.

[25] K. Uesugi, M. Hoshino, A. Takeuchi, Y. Suzuki, N. Yagi, and T. Nakano. Development of fast (sub-minute) micro-tomography. *AIP Conference Proceedings*, 1266(47):47–50, 2010.

[26] L. Borg, J. S. Jørgensen, and J. Sporring. Towards characterizing and reducing artifacts caused by varying projection truncation. Technical Report 2017/1, Department of Computer Science, University of Copenhagen, 2017. Available online: `http://static-curis.ku.dk/portal/files/174175124/Borg_2017_Towards_characterizing_and_reducing.pdf`.

[27] L. L. Barannyk, J. Frikel, and L. V. Nguyen. On artifacts in limited data spherical Radon transform: curved observation surface. *Inverse Problems*, 32(1):015012, 2016.

[28] L. V. Nguyen. How strong are streak artifacts in limited angle computed tomography? *Inverse Problems*, 31(5):055003, 2015.

[29] D. P. O'Leary P. C. Hansen, J. G. Nagy. *Deblurring Images: Matrices, Spectra, and Filtering*. SIAM, Philadelphia, USA, 2006.

[30] F. M. W. Kanters. *Towards Object-Based Image Editing*. PhD thesis, Technische Universiteit Eindhoven, Eindhoven, The Netherlands, 2007.